Hydrophobic Nanoparticles drives Budding in Mixed Bilayers

Sang Young Noh[*,†,‡] and Rebecca Notman[*,†,‡]

†*Center for Scientific Computing, University of Warwick, Coventry, Warwickshire, UK*

‡*Department of Chemistry, University of Warwick, Coventry, Warwickshire, UK*

E-mail: S.Y.Noh@Warwick.ac.uk; R.Notman@Warwick.ac.uk

Abstract

The interactions between heterogeneous components in a biomimetic bilayer controls its physical properties such as its rigidity, local and bulk curvature and propensity towards phenomena such as membrane fission and fusion. In particular, membrane proteins (MPs) and nanoparticles (NPs) have been subjects of intense interest due to their similar scale to the bilayer width and because of their ability to affect local membrane structure. However, how such NPs interact in the presence of heterogeneous aggregates in the bilayer has been the subject of much debate, especially its effect on raft-like structures. To better understand the effects of hydrophobic integration of nanoscale components on such raft-like structures, we have simulated a series of generic hydrophobic NPs interacting with a phase-separating two-component surfactant bilayer. We find that the hydrophobic NP tends to aggregate at the phase interface, acting as a line tension *relaxant* i.e. a lineactant on the phase separated interface, which results in differing demixing behavior. In particular, we demonstrate that depending on the size of the NP, the effect of the line tension can drive the a cap/bud formation around the NP, ultimately resulting in the formation of a NP-micelle structure.

Introduction

Lipids and similar polyether/polyethylene type molecules form the building blocks of a whole range of materials ranging from traditional manufacturing ingredients such as detergents and paints,[1] to more recent, complex, applications such as in bio-sensing devices, drug delivery capsules and biomedical apparatus.[2–6] Whether the lipid/polymer is biological or artificial, its basic building blocks comprises of short hydrophilic headgroups and longer hydrophobic tails. Attaching these different groups into a single lipid type species, allows the aggregation of these molecules - the hydrophilic headgroups can associate with the surrounding bulk water surrounding it, and the water-avoiding hydrophobic tailgroups aggregate away from the headgroup and water. Depending on the structure and the molecular species which make up the lipid/polymer moiety, the bulk structure can form a large array of structures ranging from a monolayer micelle to a semi-flexible planar bilayer or a bilayer vesicle. Within these bilayers, heterogeneous components can control the overall physical characteristics, such as the curvature, rigidity and permeability. Bilayers also constitute the semi-permeable vesicles that build the major organelles within biological organisms.

The preferential interactions between the molecular components, due to steric preference or direct intermolecular energetic preference has been hypothesised to drive numerous complex processes within the bilayer. The pioneering work by Simons and Ikonen[7] illustrated the possible existence of *lipid rafts* - structures ranging from 10-200 nm radius - enriched semi-circular domains that are stabilised by heterogeneous components, forming what are known as liquid-ordered (l_o) phases (which primarily make up the raft formation) from the liquid-disordered (l_d) components. The formation of patches in a mixed bilayer has been suggested to form the platform for complex macro-structures, such as membrane proteins to control the translocation of particles and ions across the bilayer.[8] In general, it is thought that the energetic cost of the raft formation depends on two main factors - the free energy gain when like lipid species coagulate together (either through packing energy or hydrophobic interaction match), and secondly, minimisation of the free energy cost of the domain boundaries. It has

been suggested that the hybrid lipid species (with a saturated and unsaturated tail), such as monosaturated POPC may control the type and size of the domains formed, through a controlled 'loosening' of the membrane domain line tension. Other stabilising factors include the presence of cholesterol (CHOL), which aggregates to the saturated tailgroups, therefore acting as a stabilising element to l_o phases.[9]

The presence of raft-like structures have yet to be demonstrated beyond doubt. Lingering issues remain in terms of lifetime within a membrane, and the minimum and maximum sizes of domains that may form, but an increasing number of experimental and simulation studies show mounting evidence of their existence. For example, the evidence for lipid rafts was shown with fluorescence spectroscopy experiments with giant unilamellar vesicles (GUVs) by Baumgart *et al*,[10,11] where a 3 component (DSPC/DOPC/CHOL) mixed bilayer showed an abrupt increase in the raft formation - from modulated patterns to macroscopic round domains with a minor increase in the DOPC ratio in rapid order. In the past, Lawrence and Yuan[12,13] showed through atomic force microscopy (AFM) that phases increasing step-wise in thickness existed within heterogeneous membranes. More recently, Nickels *et al*[14] used neutron scattering length density (NSLD) and small angle neutron scattering (SANS) techniques to 'color' the lipid components (by labelling the hydrogens on the lipids with hydrogen or deuterium atoms depending on its saturation type), which demonstrated that domain-like (l_o) features had distinctive bending moduli.

With the increasing amounts of experimental data for rafts, molecular simulation techniques have been used to reproduce the formation of such rafts. Hakoyoban *et al*[15] for example, used coarse-grained molecular dynamics (CG-MD) with the *MARTINI*[16] force field to systematically study a ternary 1,2-dioleoyl-sn-glycero-3-phosphocholine/1,2-dilauroyl-sn-glycero-3-phosphocholine/cholesterol (DOPC/DLPC/CHOL) system, with added variations in the headgroup and tailgroup regions. The study suggested that the rigidity of lipid/cholesterol species has a significant effect on stabilising/slowing the phase separation between l_o and and l_d species in a heterogeneous lipid bilayer system, which closely follows experimental obser-

vations. In addition, the interaction of raft-like aggregates with MPs seems to suggest that these can modulate the rate of phase separation. For example, Fowler et al[17] demonstrated through molecular simulation that the distribution and density of peripheral membrane proteins can change the bending rigidity. Hence, the domain formation in unsaturated/saturated mixtures have shown to be slowed by the presence of such 'linking' proteins, where it can reduce the unfavourable contact in the interface between the l_o and l_d phases.[17] In addition, hybrid lipid structures (lipids with both saturated and unsaturated tails) has been shown to act in a similar way. For example, Rosetti et al[18] demonstrated through quarternary mixtures of PAPC(hybrid)/DAPC(unsaturated)/DPPC(saturated)/CHOL mixtures that hybrid lipid type structures reduce the hydrophobic mismatch area between the l_o and l_d regions. Furthermore, all-atomic (AA) simulation results by Hassan-Zadeh et al[19] demonstrated that POPC/PLPC/PAPC type lipids essentially 'even-out' the physical characteristics between the l_o and l_d phase, which effectively reduced the domain line tension. Hence, the primary role of line tension relaxants (otherwise referred to as lineactants) is believed to be modulating the rate of phase separation by reducing the contact surface between the unfavourable components.

Hence, when designing practical applications to work in these complex environments, the interaction between any object and its interaction with the individual components, and larger structures such as these lipid rafts become an important factor to consider. Due to their potential for applications such as targeted drug-delivery, and their high bio-compatibility, nanoparticles (NPs), nanometer-scale objects of various radius and anisotropy, have recently been a subject of intense interest in relation to their application with bilayer systems. As indicated from past studies, the primary driving force for the phase separation into l_o rafts and l_d is the line tension between the phases. NPs with hydrophobic characteristics have been shown to act in a similar manner. For example, Barnoud et al[20] observed that domain stability depends on the presence of aliphatic species/NPs (Octane, Hexadecane, Cyclohexane) near the l_d/l_o domains. In addition, through mesoscopic simulations, Cheung[21] also demonstrated the control of raft-like domains with mesoscale-dynamics in the presence of hydrophobic NPs, suggesting that

4

a hydrophobic NP and a hydrophobic protein analogue can nucleate domains and act as line-actants, in a similar manner to membrane proteins. However, to the authors best knowledge, the size-dependent effects of hydrophobic NPs upon the rate and type of phase separation has not been studied before. In our work, we simulate a mixed bilayer with a hydrophobic NP of a series of increasing sized radius. We designed a *continuum* model of a hydrophobic NP to model the effects of a nanoscale hydrophobic component in a deliberately phase-separated biomimetic surface. We show that the rate of phase separation increases with a larger radius, and we also show that the NP of all sizes locates itself within the interfaces between the phases. In addition, we show that with larger radius, the NP drives a budding process that may lead to the formation of caps to a full-fledged budding.

Methods

Simulation Parameters

All simulations were performed using the *LAMMPS* molecular dynamics package.[22] To generate the initial configuration of the bilayer, 3500 CG-beads of the $C_{12}E_2$ were used to arrange a bilayer in a simulation box ranging from dimensions 80 Å $\times$ 80 Å $\times$ 200 Å with the rest of the box being filled with 14328 water beads. This system was equilibrated using a *NVT* ensemble for 1 ns simulation time with increasing timesteps to ensure the overlaps between molecules were resolved and to ensure the system did not fluctuate substantially. To reduce the likelihood of finite size effects, the simulation box was replicated once in each of the *x* and *y* directions, meaning that the simulation box was expanded from 80Å $\times$ 80 Å $\times$ 200 Å to 160 Å $\times$ 160Å $\times$ 200Å. 14000 CG beads of the $C_{12}E_2$ were used to construct the larger bilayer, which equals to 2000 molecules. This new system was also subjected to 1 ns of *NVT* equilibration in the same manner as the smaller bilayer. To insert the NP, the water beads were removed, the simulation box dimension in the direction normal to the bilayer (z-direction) was set to 200 Å and the NP was inserted into the system 100 Å above the centre of mass of the bilayer followed

by re-solvation. For productions runs, the system was simulated in the NPT-ensemble, with temperature and pressure set to 303 K and 1 atm respectively. The temperature and pressure were controlled using a Nosé-Hoover thermostat and barostat,[23][?] both with relaxation times of 0.2 ps. The equations of motion were integrated using the rRESPA multiple-timestep algorithm[25] with a 2.0 fs inner (bonded) and 10.0 fs (non-bonded) outer timesteps. Non-bonded interactions were truncated at $r_{\text{cut}} = 15$ Å. Periodic Boundary Conditions (PBCs) were set in the *x* and *y* directions. A test run of 200 ns was run to ensure that the surfactant bilayer had reached consistency in it's properties with past experimental and simulation results. This was followed by the production run over 1000 ns in the NPT ensemble.

Coarse-grained Model

In this work, we use the Shinoda-DeVane-Klein (SDK) coarse-grained (CG) model[26,27] (more recently updated to SPICA[28]). The polyethylene glycol ($C_{12}E_2$) model used by Shinoda *et al*[26,27] was the basis of the model used in this work. The model has been parameterized against thermodynamic properties (densities, interfacial tensions, transfer free energies) and has been applied successfully by itself or as a model to study a range of soft matter systems.[29–31] A brief description of their coarse-graining approach follows here - within this model 3-5 heavy atoms are represented by a single interaction site or "bead" (one water bead represents three water molecules). The system in this study consisted of a single NP, a non-ionic surfactant bilayer consisting of 2000 poly(oxyethylene) (denoted $C_{12}E_2$) surfactant molecules and 57312 water beads. The surfactant molecule was described using four CG bead types: OA (-CH_2OH) and EO (-CH_2OCH_2-) which represent the hydrophilic head group and CM (-$CH_2CH_2CH_2$-) and CT2 ($CH_3CH_2CH_2$-), which represent the hydrophobic tail groups. A schematic of the atomistic to CG mapping is given in Figure 1. To produce a mixed bilayer, half of the $C_{12}E_2$ molecules were changed into modified equivalents, which has identical *molecular mechanical* (MM) (i.e. the intramolecular potentials are identical) properties. This initial configuration was produced by a randomized change of indices atoms of the bilayer data file. The
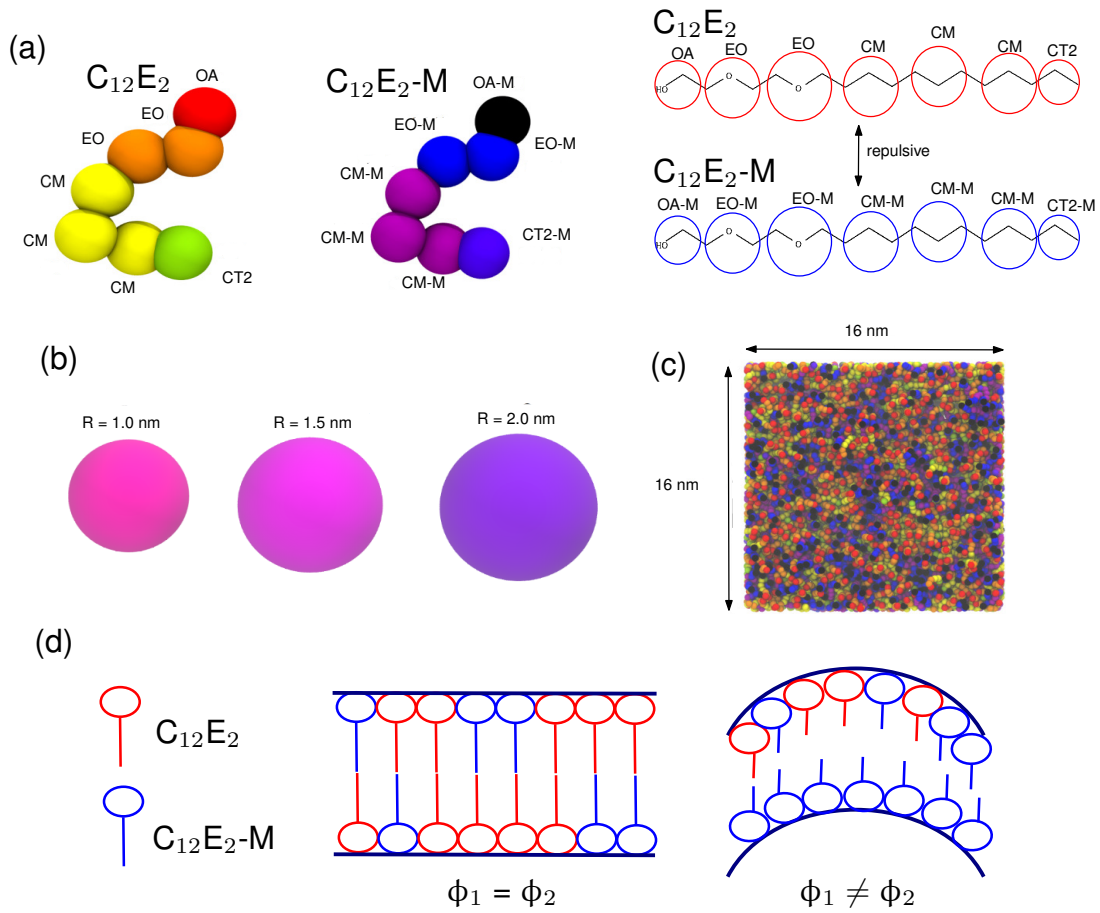
Figure 1: (a) show the schematic and CG mapping of the $C_{12}E_2$ and the $C_{12}E_2$-M surfactants, and (b) shows the schematics and sizes of the hydrophobic NPs. (c) show the top-down starting configuration and dimensions of the surfactant bilayer. (d) shows the scenario where the top and bottom monolayer are well-mixed, which is equivalent to the top (1) and bottom (2) monolayer composition being equal ($\phi_1 = \phi_2$), and the case where the one monolayer is significantly more domain-like ($\phi_1 \neq \phi_2$).

modified lipid was produced by changing the *Lennard-Jones* (LJ) ϵ values for the non-bonded potentials between surfactant and mimic beads - the LJ parameters were changed so that we could produce system which show a self-preferential phase separation to take into account the large variety of phase separation mechanisms which can be seen in real lipid bilayers. The tabulated values for these systems are shown in the supplementary information. The schematic for this modification is shown in Figure 1. The non-bonding potentials between the $C_{12}E_2$ and $C_{12}E_2$-M has been modified to show a greater extent of intermolecular repulsion between the original and mimic beads.

Model of the NPs

The NPs were treated as a collection of uniformly distributed interaction sites i.e. the particle was treated as a surface-to-molecule potential, based upon Hamaker's model for modelling the non-bonding potential of surfaces.[32,33] To represent the hydrophobic NPs, the interaction sites of the particle took the LJ parameters of the bead type CT2; the interactions between the NP and CG beads were derived from integrating the interaction potential between a CG bead and an interaction site within the NP over the particle's volume. Assuming that the interaction between a CG bead and single interaction site can be described through the modified LJ functions (Equations 1 and 2) the interaction between a NP and a CG bead may be written as

$$U_{NP}^{12-4}(r,R) = \frac{2\sqrt{3}\pi\rho\epsilon\sigma^{12}R^3}{15}\frac{5R^6 + 45R^4r^2 + 63R^2r^4 + 15r^6}{(r^2-R^2)^9} - \frac{3\pi\rho\epsilon\sigma^4 R}{r^2-R^2} + \frac{3\sqrt{3}\pi\rho\epsilon\sigma^4}{2r}\ln\left[\frac{r-R}{r+R}\right]$$

(1)

$$U_{NP}^{9-6}(r,R) = 9\pi\rho\epsilon\sigma^9 R^3\frac{3R^4 + 42R^2r^4 + 35r^4}{35r(r^2-R^2)^6} - \frac{9\pi\rho\epsilon\sigma^6 R^3}{r^2-R^2}$$

(2)

where ρ is the density of the NP and R is the NP radius. The density of the NP was taken to be 1000 kg m^{-3} (based on the density of water). Full derivations of these formulae are given in the supplementary information. The parameters ϵ and σ are the Van der Waals parameters for the W (hydrophilic) or CM (hydrophobic) CG beads. The interaction potential between the NP and solvent bead is taken as a simple interpolation of the hydrophilic and hydrophobic

potentials (Equation 3):

$$U_{NP}^{\text{type}}(r) = (x)U_{NP}^{\text{hydrophilic}}(r) + (1-x)U_{NP}^{\text{hydrophobic}} \tag{3}$$

where we set $x = 0$ to ensure a fully hydrophobic NP for each size. Plots of the interaction potentials of each NP are provided in supplementary information. Three R values were used for creating the NPs - R = 1.0, 1.5 and 2.0 nm. The 1.0 nm radius NP represents a NP that is comparable to the tailgroup (CM and CT2) length of the amphiphile, while the 2.0 nm radius NP represents a NP with a width that is comparable to the thickness of the bilayer, the 1.5 nm radius being the intermediate. For each R, the hydrophobic interaction between the NP and $C_{12}E_2/C_{12}E_2$-M is identical.

Membrane Domain and Budding Energetics

We have approached the problem of membrane energetics in the way as described by Wolff *et al*[34] and Lipowsky,[35,36] which involves dividing up the bending, interface and composition energetics, following on from the elastic properties of a bilayer described by Helfrich.[37] The approach entails dividing up the bilayer conformation around the domain and the NP in terms of the bending energy (the cost of increasing the curvature around the NP), the edge energy (the unfavourable energetic contribution between the domains) and the adhesion energy (the energetic cost of adhering on the NP surface). The bending energy term is defined by:

$$E_{\text{bending}} = 2\pi L^2 \kappa \left[(C - C_0)^2 + (C + C_0)^2\right] \tag{4}$$

Where κ is the bending rigidity, L is the radius of the dimple/cap, C is the curvature of the dimple/cap, and C_0 the spontaneous curvature of the bilayer. Here, we can estimate the curvature as $\frac{1}{R}$, if we assume that the center of the NP position is aligned with the peak of the cap/micelle. The energetic cost of forming the edge also needs to be taken into account - the

domain edge energy can be defined as:

$$E_{\text{edge}} = 2\pi L\gamma\sqrt{1 - (LC/2)^2} \tag{5}$$

Hence, we can define the energetic contributions of the budding formation from the surfactant itself by the sum of the bending and edge contributions:

$$E_{\text{total}} = 2\pi L\left[\left(L\kappa((C - C_0)^2 + (C + C_0)^2)\right) + \gamma\sqrt{1 - (LC/2)^2}\right] \tag{6}$$

where γ indicates the line tension. To measure γ, it is required to measure the unfavourable interaction forces at the phase interface - originating from the difference in intermolecular potentials and/or structural variations. To infer γ, we used a stabilized phase-separated system which had stabilized domain boundaries, and extracted the stress tensor components for each CG bead of the $C_{12}E_2$ and $C_{12}E_2$-M components and averaged them over the intra-planar axes i.e. the x and y axes. This is extracted from the stress tensor components from the molecules in the system. The tabulated force field parameters for the line tension computation is included in the supplementary information. The adsorption/adhesion energy $E_{adhesion}$ of the surfactants to the NP surface, as estimated by Bahrami $et\ al$[38] is computed as:

$$E_{\text{adhesion}} = -4\pi R^2 Ux \tag{7}$$

where U $\geq$ 0 is the adhesion energy per unit area, and x is the fraction of the NP area that is wrapped by the surfactant. Here, we have measured the interaction energy of the $C_{12}E_2$ and $C_{12}E_2$-M components with the NP surface. The sum of the interaction forces in the x, y and z axes can be estimated as the E_{adhesion}, which in turn can be used to infer U. A negative E_{adhesion} is responsible for the formation of the micelle/bud, while E_{bending} and E_{edge} are the equivalent to the energetic cost required. We can consider the sum of the E_{bending}, E_{adhesion} and E_{edge} as the main components due the bud/micelle formation, therefore, the total energetic contribution

to the formation of the cap/bud is given by:

$$E_{\text{total}} = E_{\text{bending}} + E_{\text{adhesion}} + E_{\text{edge}} \tag{8}$$

Estimates for the limiting domain (L_{limit}) and neck length (N_{ib}), as defined by Lipowsky, is computed by the following equations:

$$L_{\text{limit}} = \frac{8\iota}{[1 + (4\iota|C_0|)^{2/3}]^{3/2}},$$
$$N_{\text{ib}} = \frac{8\iota}{[1 + (4\iota|C_0|)^{2/3}]^2} \tag{9}$$

Where ι represents $\frac{\kappa}{\gamma}$, which represents the *invagination length*. During the formation of bud attached to the bilayer by a neck, the lateral tension imposed by the bud is estimated by:

$$\Sigma = \left(\frac{\sigma}{N}\right) - 8\kappa\frac{\left(1 - \frac{C_0}{C}\right)}{L^2} \tag{10}$$

A positive Σ value represents the bud being pulled away from the bulk surfactant membrane, while a negative value represents the bud being pulled towards the membrane.

Composition Analysis around the NPs

Wolff *et al*[34] estimated the 'incompatibility' energy (or the measure of the tendency of each bilayer component to disaggregate) from the Landau expansion of the monolayer composition, which is highly dependent on the monolayer compositions of the bilayer, which in turn affects the magnitude of the spontaneous curvature. A flat bilayer domain may become spontaneously curved whenever an excess of a single lipid component is highly concentrated in a patch of the monolayer. Here, the exact composition energy is difficult to extract, as the interaction energy near the domain region cannot be easily extracted, and while the interaction energy between the $C_{12}E_2$ and $C_{12}E_2$-M can be computed, this does not guarantee its relevance as the incompatibility energy. Instead, following the convention followed by Wolff, we have computed

the monolayer compositions ϕ_1 and ϕ_2 (indices 1 and 2 representing each monolayer) around the NP in a 8 nm radius around the NP, to modify the composition dependent spontaneous curvature:

$$\phi_1 = \phi_1^{C_{12}E_2} - \phi_1^{C_{12}E_2\text{-}M} \tag{11}$$

$$\phi_2 = \phi_2^{C_{12}E_2} - \phi_2^{C_{12}E_2\text{-}M} \tag{12}$$

Hence, we can compute the average composition of both monolayers as:

$$\phi_{av} = \frac{\phi_1 + \phi_2}{2} \tag{13}$$

The composition difference was averaged for every 1 Å intervals away from the NP center. Each of the monolayer compositions around the NP region was analysed to measure how the interaction of the surfactants of the bilayer affected the local compositions around the NP. Hence, by analysing this composition data, we can estimate the extent during incompatibility near the NP region, and the 'lifetime' which this 'incompatible' conformation remains around the NP.

Table 1: Simulation parameters for each mixed bilayer/NP simulation

NP size (nm)	$C_{12}E_2$ (N)	$C_{12}E_2$-M (N)	t (ns)	x × y (nm^2)
-	1000	1000	1000	16 × 16
-	1000	1000	1000	16 × 16
1.0	1000	1000	1000	16 × 16
1.5	1000	1000	1000	16 × 16
2.0	1000	1000	1000	16 × 16

Table 2: Energetic parameters values used for curvature calculations.

NP size (nm)	C (nm^{-1})	γ (N)	$\frac{\kappa}{\sigma}$ (nm)	$A_{NP_{cap}}$ (nm^2)	L (nm)	LC
1.0	0.357	1×10^{-12}	22.59	11.32π	2.8	0.9996
1.5	0.303	1×10^{-12}	22.59	15.79π	3.3	0.9990
2.0	0.2	1×10^{-12}	22.59	20.85π	3.8	0.7600

Results and Discussion

Mixed Bilayer Systems with/without the NPs

Table 1 shows the tabulated simulations involved in this work. Figure 2 (a) show the snapshots of the $C_{12}E_2$/$C_{12}E_2$-M with the R = 1.0, 1.5 and 2.0 nm radius simulations. We have observed that in these cases, the NPs remain within the hydrophobic interior of the bilayer. We did not observe any significant budding or fission processes with the monolayer. The mixed bilayer system without the NPs is shown in Figure 2 (b). We see that significant phase separation occurs after 800 ns, we see an increase in the curvature of the bilayer corresponding to a greater phase separation. The analogous simulation with the hydrophobic NPs for R = 1.0, 1.5 and 2.0 nm are shown in Figures 2(b), (c) and (d) respectively. With the entry of the NP into the bilayer center we see the formation of a cap for the R = 1.0 nm example (at 500 ns), and a full budding/micelle formation in the case of the R = 2.0 nm example. The R = 1.5 nm shows the intermediate case, showing the formation of a significant cap around the NP. By measuring the the density of each type of surfactants around the NP, we can measure the dynamic change in the conformation of the cap/bud.

Membrane Budding and Micelle Formation - The Relation between the Line Tension and the NP

Figure 4 (a) show the RDF profiles of the $C_{12}E_2$ and $C_{12}E_2$-M components around each NP. For all the NP samples, we see a direction of change in the density profile, where a decrease in the $C_{12}E_2$ peaks corresponds to a $C_{12}E_2$-M peaks within 2 nm of the NP surface, which suggests a dynamic change of the surfactant conformations on the NP surface. From distances of 4 nm to 10 nm, we observe a significant trough forming which is most exaggerated in the case of the R = 2.0 nm, which corresponds to the budding of the NP. Figure 4 (b) shows the $E_{adhesion}$ computation for each system. From this, we can approximate the $E_{adhesion}$ as the sum of the $C_{12}E_2$/$C_{12}E_2$-M contributions, which approximates to, on average, values in the ranges

of -25 - 50, -50 - -75 and -75 - -150 kcal mol^{-1} for the R = 1.0, 1.5 and 2.0 nm examples respectively. In each case, we see a negative adhesion energy which favours the wrapping of the NP.[38] As it is apparent from simulation snapshots that each NP is fully wrapped by the surfactant components (hence, x is simply the surface area of the NPs, which are 12.57, 28.27 and 50.27 nm^2). As it is apparent from simulation snapshots that each NP is fully wrapped by the surfactant components (hence, x is treated a unity, as it represents the fraction of the NP engulfed in the bilayer, and it has been completely engulfed). From equation 7, the adhesion energy per area for each NP can be approximated as 5.97 kcal mol^{-1} nm^{-2} (3.536 k$_b$T nm^{-2}), 5.30 kcal mol^{-1} nm^{-2} (3.143 k$_b$T nm^{-2}), and 3.979 kcal mol^{-1} nm^{-2} (2.357 k$_b$T nm^{-2}) for the R = 1.0, 1.5 and 2.0 nm NP respectively. The resulting composition profile around each NP can be analyzed over time, as seen in Figure 3. The ϕ_{av}, measured as a function of distance from the NP center, has been averaged over 1000 ns in 200 ns batches. The gradient of ϕ seems to play a key part in the budding process. For the R = 1.0 nm, We see the formation of a gradient between 4 nm and 6 nm between 600 - 800 ns, and the formation of such a gradient seems to correspond with the point in the simulation where budding does indeed occur. In the case of the R = 1.5 nm, we see similar effects with a gradient starting at 3 nm, which converges to 0 between 7 - 8 nm. Finally, for the R = 2.0 nm, we see a clear gradient formed between 4.5 - 8 nm between 0 - 400 ns. It is worth noting that the formation of a 'stable' gradient (where the composition gradient persists over the simulation time) is apparent in the case for the R = 1.5 nm and 2.0 nm, while we see a greater fluctuation in the case of the R = 1.0 nm. This supports our previous analysis in the RDF profiles, which suggests dynamic and continuous rearrangements around the NP radius on the surface of the NP. With the γ measurements (Figure 4 (c)) from the restrained NP/mixed bilayer simulations, what we see is that the presence of the NP effectively creates a platform around its radius where the γ is relaxed, as shown by the stress tensor profiles. The estimated value for γ for the length of the domain interface is 2.9607 $\times$ 10^{-12} J m^{-1}. Experimental measurements of the line tension values range in the region of 0.2-6.2 $\times$ 10^{-12} J m^{-1},[10,40] which shows that the mixed bilayer showed in this simulation is
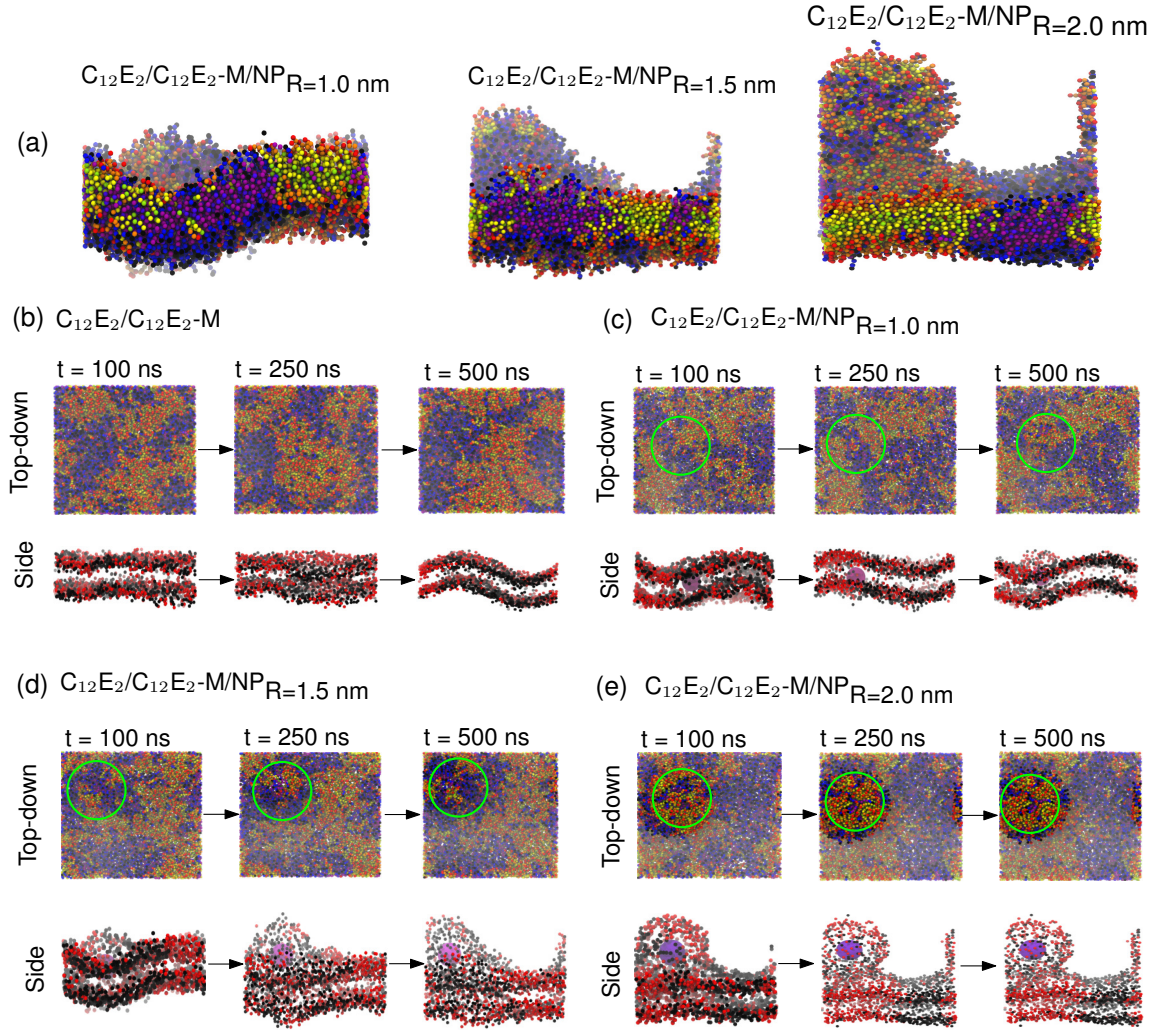
Figure 2: Trajectory snapshots for the series of simulations run in this work, over 500 ns, showing the top-down and side views. (a) shows the snapshots of the systems at 500 ns for the R = 1.0, 1.5 nm and 2.0 nm simulations, (b) shows the NP-absent simulation, (c) shows the R = 1.0 nm simulation, (d) shows the R = 1.5 nm simulation, and (e) shows the R = 2.0 nm simulations respectively. The green circles on the top-down images show the location of NP and the budding process for each simulation. All simulations were visualized using VMD[39]

15

comparable to the measurements seen with experiments. The effect of the hydrophobic NPs is such that it introduces a surface that allows the surfactant components to reorganise itself to create a domain interface *around* it, as shown by the gradual increase of the RDF plots of the $C_{12}E_2$/$C_{12}E_2$-M as a function of time. (Figure 4 (a)). If we break down the influence of the hydrophobic NP upon a mixed bilayer, the locational preference of the NP near the domain interface indicates that it is a line-active component, and hence, reflects a local reduction of the line tension.   Taking the center of the NP in each simulation as the cap/bud center, we can estimate the curvature C as $\frac{1}{2.8nm}$, $\frac{1}{3.3nm}$ and $\frac{1}{3.8nm}$ for the R = 1.0, 1.5 and 2.0 nm NPs respectively, which is equivalent to 0.357 nm^{-1}, 0.303 nm^{-1} and 0.2 nm^{-1} respectively - the schematic for these estimates are shown in Figure 3. The computed parameter values from this is shown in Table 2. The membrane budding model suggested by Lipowsky[35] showed that the competition between the domain line tension and the membrane bending energy results to a transition to either a partial or complete budding state. It has been hypothesised that once the domain region exceed a critical size, the domain can transition into a dimpled or fully budded state, or in other words, become unstable and hence undergo a invagination process driven primarily by the fluctuation in the bilayer curvature by changes in temperature. In our simulations, we observe dimpled states of differing magnitudes of curvature with the R = 1.0 and 1.5 nm NP, and a fully budded state with the R = 2.0 nm NP example. As the NPs becomes larger, the budding becomes much more significant, which would suggest that this effect would also occur with large, rigid clusters of hydrophobic NPs, which has been observed as common occurrences in nature.[41,42] Here, the contributing forces in the cap/bud formation are the unfavourable interactions between the $C_{12}E_2$/$C_{12}E_2$-M, the energetic cost of forming the cap/bud, the effect of the NP upon the local arrangement of the surfactants around it, and the extent of interaction between the NP surface and the $C_{12}E_2$/$C_{12}E_2$-M components. Figure 5 (a) shows the estimated E$_{total}$ for a range of spontaneous curvature (between 0.2 and 1.0), for the R = 1.0, 1.5 and 2.0 nm NPs present. We see that the energies range between -2.0 $\times$ 10^{-19} to 5.0 $\times$ 10^{-19} J for all sizes. The k$_b$T (energetic scale) for the simulations show an
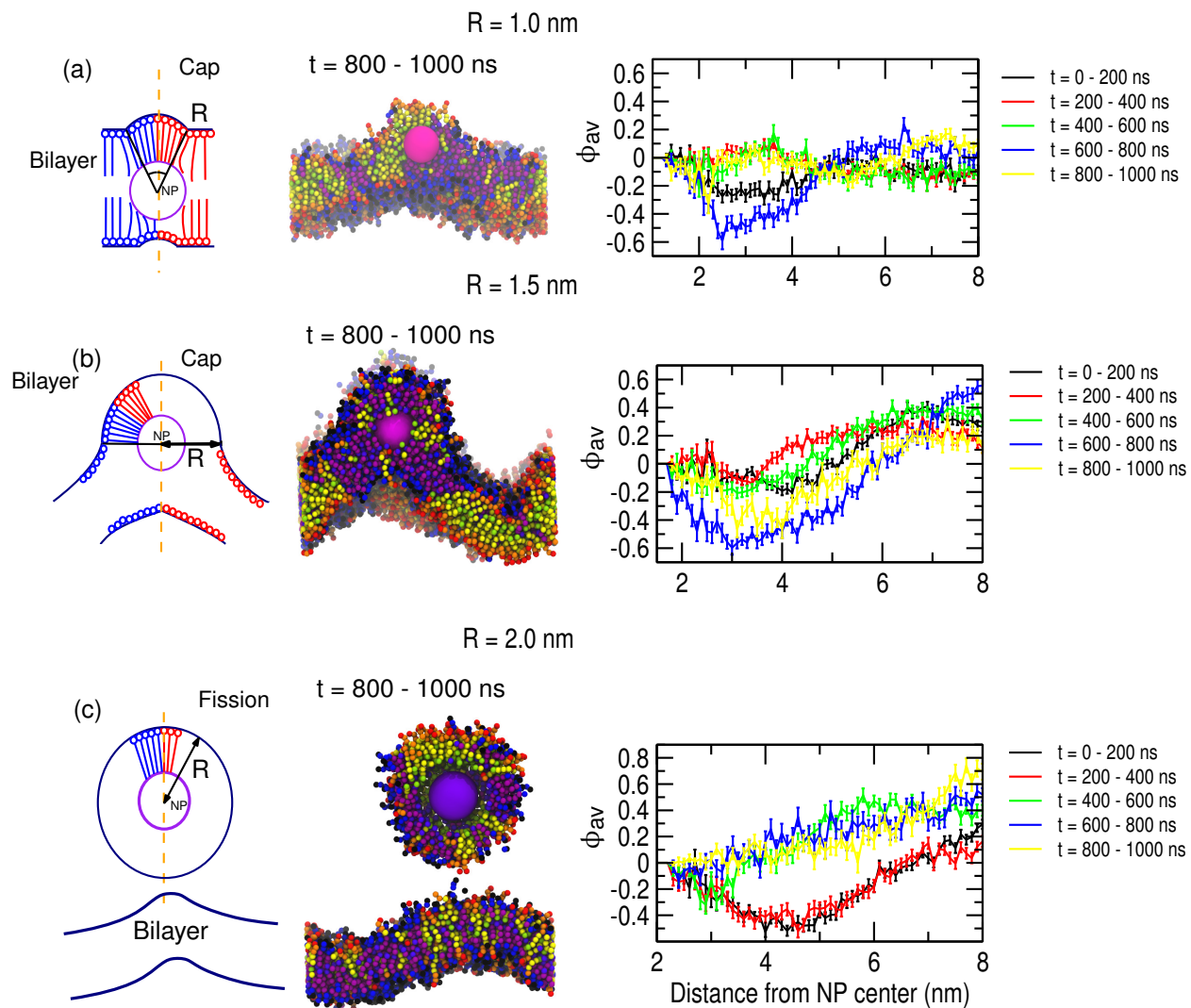
Figure 3: Schematics and snapshots showing the budding formations at between t = 800 - 1000 ns for the R = 1.0, 1.5 and 2.0 nm for (a), (b) and (c) respectively, along with the averaged composition profiles as a function of the distance from the NP center. The value of R represents the radius of the cap/bud used for the curvature computations. The ϕ values were averaged over steps of 200 ns increments. The red components shows the $C_{12}E_2$ surfactants, while the blue components show $C_{12}E_2$-M components.
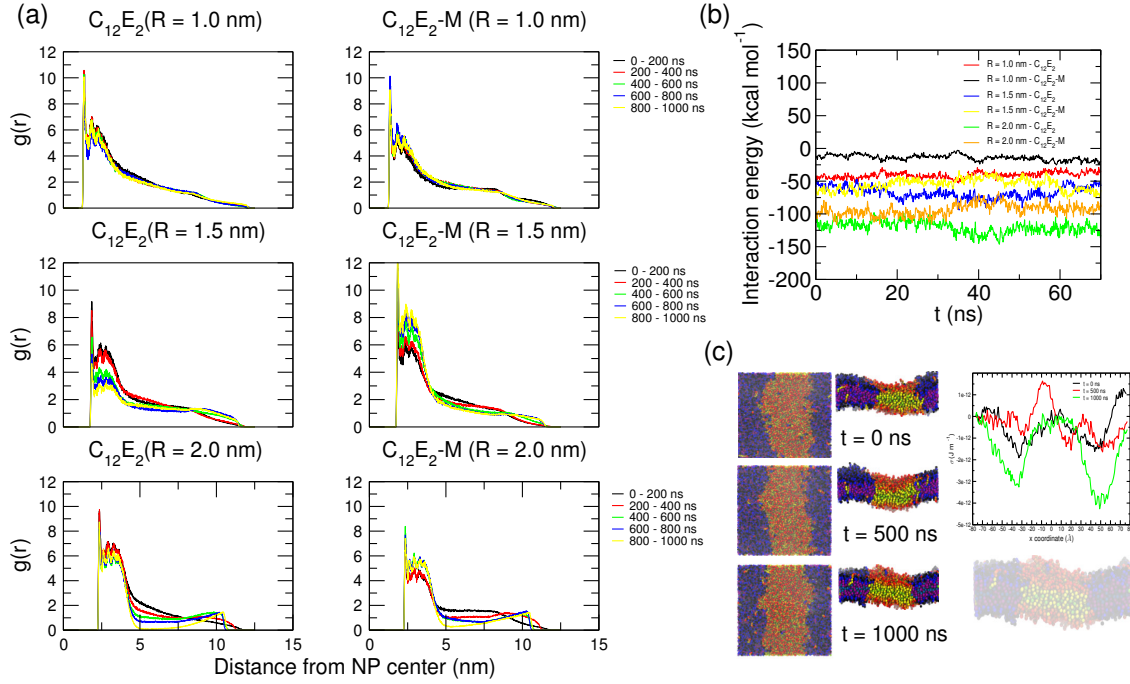
Figure 4: (a) shows the changes in the RDF profiles of the $C_{12}E_2$ and $C_{12}E_2$-M as a function of distance from the NP center, for the R = 1.0, 1.5 and 2.0 nm simulations, (b) shows the computed interaction energy between the $C_{12}E_2/C_{12}E_2$-M residues and the NP over 70 ns, while (c) shows the line tension (γ) measurement from a well-separated phase separated system of $C_{12}E_2/C_{12}E_2$-M, averaged at 3 timesteps.
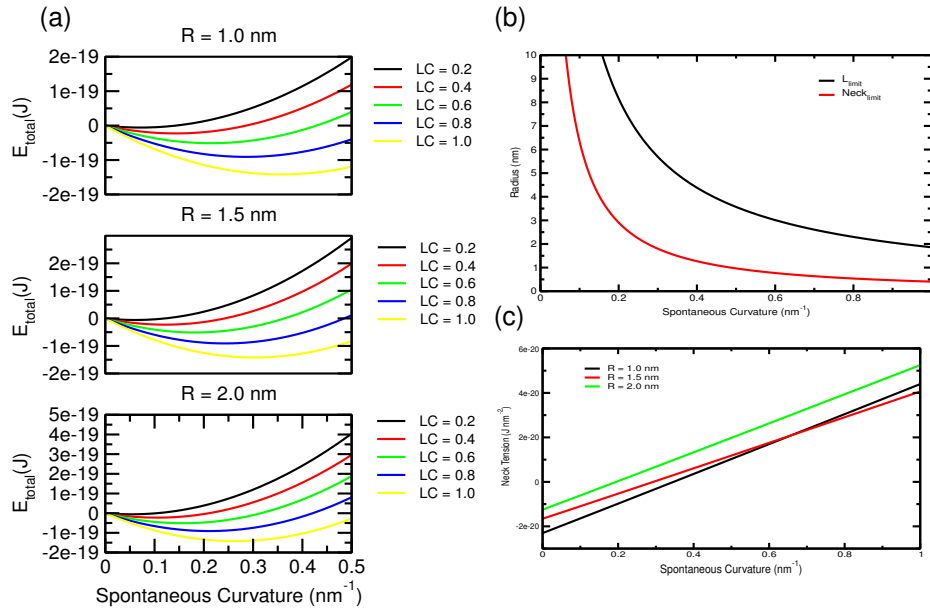

Figure 5: (a) shows the plots for E_{total} for differing spontaneous curvatures (C_0) and LC values. (b) shows the limiting L and fission neck radii for different values of the spontaneous curvature. (c) shows the neck tension as computed by equation 10 for the budding/invagination process

estimate of 4.1814×10^{-21} J, which would suggest within our model mixed bilayer budding would not occur simply through thermal fluctuations, as we see with our examples with the NP-absent simulations. Figure 5 (b) shows the predicted L_{limit} and $Neck_{limit}$ with the parameters as measured with this system. If we approximate the maximum spontaneous curvature that can be taken to be between 0.2 - 0.4 (the range of the curvature that is induced by the NPs) we see that there is a theoretical neck radius of 1 - 3 nm, and the L_{limit} of 4 - 9 nm. The neck tension (Figure 5 (c)) shows a range between 1.5×10^{-20} and 1.8×10^{-20} J nm^2, which indicates that there is a positive neck tension and shows that the bud pulls the surrounding region. It is noticeable that the energies related to bilayer curvature invagination is much lower compared to the $E_{interaction}$ estimations, which may imply that the NP interaction reinforces the budding mechanism. Figure 6 (a) and (b), shows the changes in the pressure tensor components across the system normal, while (c) and (d) shows the averaged pressure tensor components on the lateral plane of the surfactant bilayer. Overall, the trend we see is that along the bilayer normal is the P_{yy} and P_{xx} components being reduced through the budding process, and that the P_{xx} component along the lateral plane show regions of high tension around the NP, which also highlights its correlation with the composition gradient formed around the NP for each of the simulation. Figure 7 illustrates the mechanism; the distinguishing factors for larger NPs (especially prevalent in the R = 2.0 nm example) is that there is a greater surface area for the surfactants to adsorb onto the surface, while for the smaller NPs, steric hindrance between the surfactants and its effect of being a 'smaller' lineactant (i.e. the surface area around the NP of which the line tension is relaxed is smaller). The lineactant effect of the hydrophobic NPs can be seen in other studies. Palmieri *et al*[43] showed through ternary composition bilayer simulations that line-active components are observed to accumulate on the binary interface, and following the language of Hassan-Zadeh *et al*,[19] we can conclude that the hydrophobic NP acts as a 'loosening' type of lineactant, compared to hybrid lipids which may act to decrease the line tension by partitioning inside the domain structure. This effect is most likely not contained within simply NPs - Jeffrys *et al* for example, suggested that in the presence of
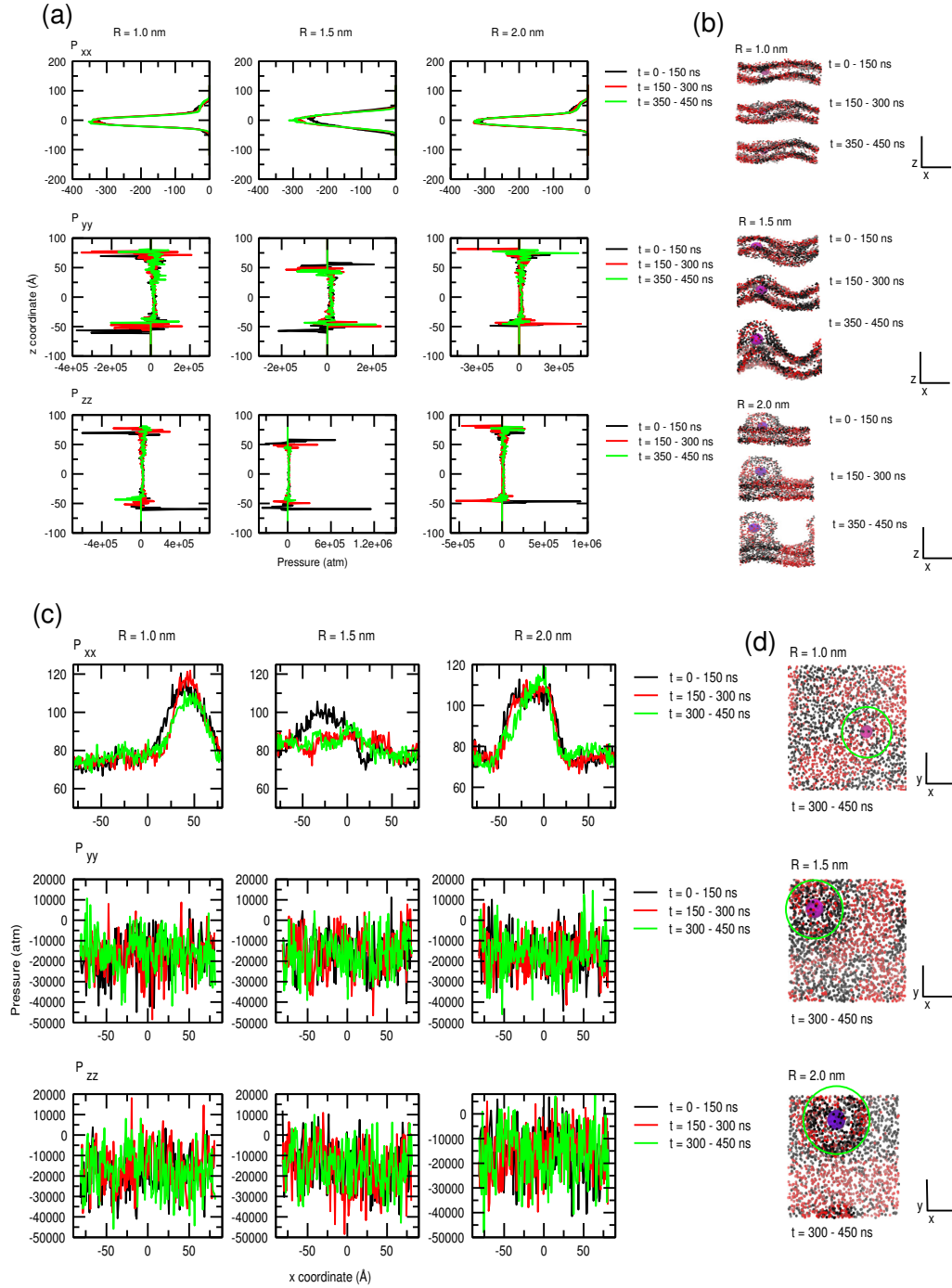
Figure 6: (a) shows the averaged pressure profiles for the P_{xx}, P_{yy}, P_{zz} along the x axis, averaged for every 1 Å increments, for each 150 ns batches up to 450 ns. (b) shows the snapshot profile corresponding to the pressure profiles. (c) shows the averaged pressure profiles for the P_{xx}, P_{yy}, P_{zz} along the z axis, averaged for every 1 Å increments, for each 150 ns batches up to 450 ns, (d) show the snapshot of the system at 450 ns, where the green circle indicates the indicates the region where the NP is present.
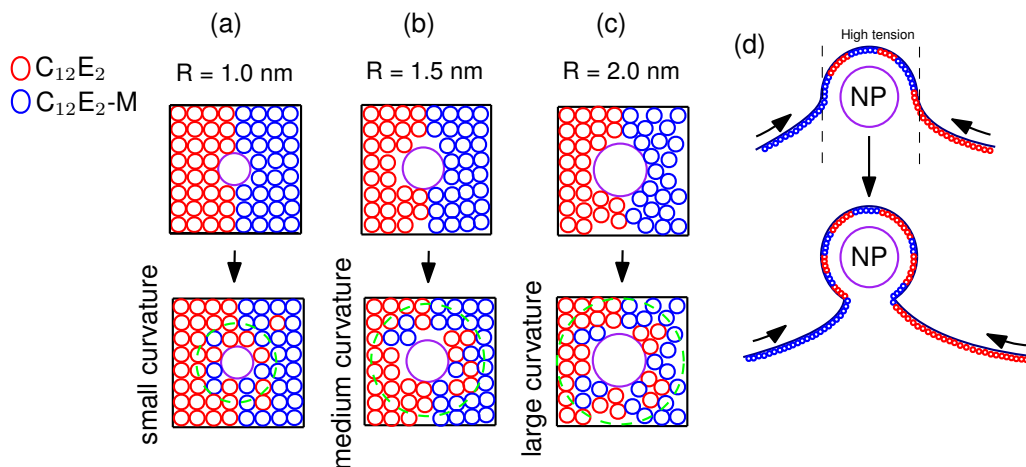
Figure 7: The schematics for the composition of $C_{12}E_2$ and $C_{12}E_2$-M around each NP through the budding process. (a), (b) and (c) show the composition arrangement for the R = 1.0, 1.5 and 2.0 nm respectively. The green circles indicate regions where $\phi_1 \neq \phi_2$, and therefore has the highest spontaneous curvature. (d) shows the budding process with the R = 2.0 nm NP, where the local stress induced by the nanoparticle due to composition mismatch and increase of unfavourable contacts between the surfactants drive the fission process.

the membrane-associated G-protein NRas, the rate of domain formation/phase separation in a tertiary bilayer was shown to be dampened,[17] which is consistent with its hypothetical effect as a line active component in a mixed bilayer. This interface nucleating effect of hydrophobic NPs has been replicated by Cheung[21] using *dissipative particle dynamics* (DPD) simulations, and from this simulation, we see that the nucleation is initially driven the hydrophobic attraction between the NP and each of the lipid/lipid mimic components, and in large numbers, clustering of NPs along the interface has been shown to affect the size of the rafts formed in the simulations. The hydrophobic interface provided by the NP here can be compared to the binding motifs on proteins such as the HIV glycoprotein (HIV-GP41), which binds specifically to CHOL molecules,[44] whilst other proteins have been known to bind to sphingolipids and sphingomyelin components.[45,46] In previous studies, Ruiz-Herrero *et al*[47] analyzed the assembly of viral capsids on small membrane domains, and indicated that the domains provide sites of budding due to reduced free energy penalties associated with budding; the adsorption of viral capsomer models preferentially interacts with the lipid domain, and subsequent budding is induced as increased curvature reduces the length of the domain interface, and the com-

pressive force arising from the domain surrounding the neck also driving the budding. Other viral budding studies by Lazaro et al[48] showed that for viral capsids, which are significantly larger than these NPs (> 100 nm), glycoprotein (GP) embedding provided the environment for budding mechanisms, which may indicate that the mechanism shown in this work may only be applicable with much smaller particulates (< 10 nm). However, recent experimental studies by Yang et al[49] indicated that HIV-GP41 mimic subunits do fuse preferentially to the edges of cholesterol rich lipid domains. In other studies, Madsen et al[50] used molecular simulations to find that the influenza A M2 transmembrane proteins act as an inducer and a sensor for local curvature, and lines up near the sites of line tension/domain interface, to reduce the tensile and compressive stresses in the bilayer due to its conical shape. Reflecting on this work, we hypothesise that the local reduction of the line tension drives the initial entry of NP/glycoprotein structures. However, the mismatch of lipid components between the membrane leaflets in the region around the NP/glycoprotein induces high lateral stress, which produces curvature.

We are aware that the key weakness of this study is that the mixed bilayer does not represent a single type of bilayer. For example, experimental studies using neutron scatter measurements detected distinctly separate bending moduli in lateral heterogenities.[14] Also, for certain mixed compositions, we observe drastically varying bending moduli in mixed bilayers,[51] ranging from 30 (l_d phases) to 100 k_BT (l_o phases) - of an order of magnitude larger than the bending rigidity observed for this study (5.4 k_BT). Other studies indicates complementary, yet differing effects of lineactants. For example, Li et al[52] showed that hybrid lipid-like lineactant molecules aggregates near the domain boundaries of vesicles, indicating a clear reduction in the local line tension, acts to reduce the curvature near the domain boundary. However, this study does follow previous studies in showing that the hydrophobic NP does act as a lineactant in the presence of local raft-like structures in heterogenous lipid bilayers, and it could be considered an limiting case of NP/proteins interacting with domain interfaces. From this theoretical study, it is clear that with a spherical NP, the interplay between the bending energy associated with the membrane curvature around the NP, and the adhesion energy due to favourable hy-

drophobic interaction is disrupted when placed in a multicomponent bilayer. We hypothesize that full budding only occurs with the R = 2.0 nm as adhesion energy between the NP and the surfactants are not sufficient in the cases of the R = 1.0 and R = 1.5 nm NPs.

Conclusion

We have used molecular dynamics simulations to compute the interactions of a continuum model of hydrophobic hamaker-model NPs with a mixed surfactant bilayer and have noted a novel surfactant budding mechanism, with increasing NP radius. The lineactant hydrophobic NP induces a gradient of 'mismatch' as the NP radius increases, which materializes as significant composition difference between the monolayers. As seen from estimating the bending and edge energies, these energies do not differ significantly between each NP size, which suggests that the adsorption energy on the NP surface and the increase in the spontaneous curvature (due to the suppressed membrane remodelling around the NP) around the NP is the primary driver for the cap/budding of the NP. As indicated in this studies, the spherical particle budding in mixed bilayer/capsid systems is due to the buckling of the line tension interface to reduce the length of the domain interface.[35] From this, we can conclude that within the simulations shown in this study, the effect of the NPs size is to increase the line tension along the domain interface, which results in the partial/complete budding depending on the radius. The formation of a mismatch gradient from the distance of the NP center seems to be the primary driver for this - this can also be inferred as a fully phase-separated bilayer forms from the aftermath of the budding. This mechanism demonstrates that the sites of membrane line tension in phase separated bilayers may act as a marker for hydrophobic species to conglomerate and as a catalyst for budding events, and requires further investigation.

References

(1) Baumgart, T.; Hess, S. T.; Webb, W. W. Imaging coexisting fluid domains in biomembrane models coupling curvature and line tension. *Nature* **2003**, *425,* 821–824.

(2) Zhou, W.; Burke, P. J. Versatile Bottom-Up Synthesis of Tethered Bilayer Lipid Membranes on Nanoelectric Biosensor Devices. *ACS Applied Materials & Interfaces* **2017**, *9,* 14618–14632.

(3) Dimov, N.; Kastner, E.; Hussain, M.; Perrie, Y.; Szita, N. Formation and purification of tailored liposomes for drug delivery using a module-based micro continuous-flow system. *Nature Scientific Reports* **2017**, *7*.

(4) Inci, F.; Celik, U.; Turken, B.; Ozer, H.; Kok, F. Construction of P-glycoprotein incorporated tethered lipid bilayer membranes. *Biochemistry and Biophysics Reports* **2015**, *2*, 115 – 122.

(5) Mazur, F.; Bally, M.; Stadler, B.; Chandrawati, R. Liposomes and lipid bilayers in biosensors. *Advances in Colloid and Interface Science* **2017**, *2*.

(6) Petaccia, M.; Bombelli, C.; Sterbini, F. P.; Papi, M.; Giansanti, L.; Bugli, F.; Sanguinetti, M.; Mancini, G. Liposome-based sensor for the detection of bacteria. *Sensors and Actuators B: Chemical* **2017**, *248*, 247–256.

(7) Simons, K.; Ikonen, E. Functional rafts in cell membranes. *Nature* **1997**, *387*, 569 – 572.

(8) Meer, G. V.; Voelker, D. R.; Feigenson, G. W. Membrane lipids: where they are and how they behave. *Nature Reviews* **2008**, *9*, 112 – 124.

(9) Schmid, F. Physical mechanisms of micro- and nanodomain formation in multicomponent lipid membranes. *Biochimica et Biophysica Acta* **2016**,

(10) Heinrich, M. C.; Levental, L.; Janmey, P. A.; Baumgart, T. Critical Exponents for Line Tension and Dipole Density Difference from Lipid Monolayer Domain Boundary Fluctuations. *Journal of Physical Chemistry B* **2008**, *112*, 8063 – 8068.

(11) Usery, R. S.; Enoki, T. A.; Wickramasinghe, S. P.; Weiner, M. D.; Tsai, W.; Kim, M. B.; Wang, S.; Torng, T. L.; Ackerman, D. G.; Heberle, F. A.; Katsaras, J.; Geigenson, G. W. Line Tension Controls Liquid-Disordered + Liquid-Ordered Domain Size Transition in Lipid Bilayers. *Biophysical Journal* **2017**, *112*, 1431 – 1443.

(12) Lawrence, J. C.; Saslowsky, D. E.; Edwardson, J. M.; Henderson, R. M. Real-time analysis of the effects of cholestrol on lipid raft behavior using atomic force microscopy. *Biophysical Journal* **2003**, *84*, 1827 – 1832.

(13) Yuan, C. B.; Furlong, J.; Burgos, P.; Johnson, L. J. The size of lipid rafts: an atomic force microscopy study of ganglioside GM1 domains in sphingomyelin/dopc/cholestrol membranes. *Biophysical Journal* **2002**, *82*, 2526 – 2535.

(14) Nickels, J. D.; Cheng, X.; Motofian, B.; Stanley, C.; Lindner, B.; Herberle, F. A.; Perticaroli, S.; Feygenson, M.; Egami, T.; Standert, R. F.; Smith, J. C.; Myles, D. A. A.; Ohl, M.; Katsaras, J. Mechanical Properties of Nanoscopic Lipid Domains. *ACS Nano* **2014**, *8*, 2161–2175.

(15) Hakobyan, D.; Heuer, A. Key Molecular Requirements for Raft Formation in Lipid/Cholesterol Membranes. *Plos One* **2014**, *9*, e87369.

(16) Marrink, S. J.; Risselada, H. J.; Yefimov, S.; Tieleman, P. D.; de Vries, A. H. The MARTINI Force Field: Coarse Grained Model for Biomolecular Simulations. *Journal of Physical Chemistry B* **2007**, *111*, 7812–7824.

(17) Jefferys, E.; Sansom, M. S. P.; Fowler, P. W. NRas slows the rate at which a model lipid bilayer phase separates. *Faraday Discussions* **2014**, *169*, 209–223.

(18) Rosetti, C. M.; Montich, G. G.; Pastorino, C. Molecular Insight into the Line Tension of Bilayer Membranes Containing Hybrid Polyunsaturated Lipids. *Journal of Physical Chemistry B* **2017**, *121*, 1587 – 1600.

(19) Hassan-Zadeh, E.; Baykal-Caglar, E.; Alwarawrah, M.; Huang, J. Complex Roles of Hybrid Lipids in the Composition, Order and Size of Lipid Membrane Domains. *Langmuir* **2014**, *30*, 1361 – 1369.

(20) Barnoud, J.; Rossi, G.; Marrink, S. J.; Monticelli, L. Hydrophobic Compounds Reshape Membrane Domains. *PLOS Comput Biol* **2014**, *10*, e1003873.

(21) Cheung, D. Aggregation of nanoparticles on one and two-component bilayer membranes. *The Journal of Chemical Physics* **2015**, *141*, 194908.

(22) Plimpton, S. Fast Parallel Algorithms for Short-Range Molecular Dynamics. *Journal of Computational Physics* **1995**, *117*, 1–19.

(23) Nose, S. A unified formulation of the constant temperature molecular dynamics methods. *The Journal of Chemical Physics* **1984**, *81*, 511.

(24) Tuckermann, M. E.; Mundy, C. J.; Martyna, G. J. *Journal of Chemical Physics* **2001**, *115*, 1678.

(25) Tuckermann, M.; Berne, B. J.; Martyna, G. J. Reversible multiple time scale molecular dynamics. *J. Chem. Phys* **1992**, *97*, 1990 – 2001.

(26) Bandyopadhyay, S.; Tarek, M.; Lynch, M. L.; Klein, M. L. Molecular Dynamics Study of the Poly(oxyethylene) Surfactant C12E and Water. *Langmuir* **2000**, *16*, 942 – 946.

(27) Shinoda, W.; DeVane, R.; Klein, M. L. Coarse-grained molecular modeling of non-ionic surfactant self-assembly. *Soft Matter* **2008**, *4*, 2454–2462.

(28) Seo, S.; Shinoda, W. SPICA Force Field for Lipid Membranes: Domain Formation Induced by Cholesterol. *Journal of Chemical Theory and Computation* **2019**, *15*, 762 – 774.

(29) Alemani, D.; Collu, F.; Cascalla, M.; Peraro, M. D. A Nonradial Coarse-Grained Potential for Proteins Produces Naturally Stable Secondary Structure Elements. *Journal of Chemical Theory and Computation* **2010**, *6*, 315 – 324.

(30) Devane, R.; Klein, M. L.; Chiu, C.; Nielson, S. O.; Shinoda, W.; Moore, P. B. Coarse-Grained Potential Models for Phenyl-Based Molecules: I. Parametization using Experimental Data. *Journal of Physical Chemistry B* **2002**, *296*, 6386 – 6393.

(31) LeBard, D. N.; Levine, B. G.; Mertmann, P.; Barr, S. A.; Jusufi, A.; Sanders, S.; Klein, M. L.; Panagiotopoulos, A. Z. Self-assembly of coarse-grained ionic surfactants accelerated by graphics processing units. *Soft Matter* **2012**, *8*, 2385 – 2397.

(32) Chi-Cheng, C.; Moore, P. B.; Shinoda, W.; Nielson, S. O. Size-dependent hydrophobic to hydrophilic transition for nanoparticles: A molecular dynamics study. *The Journal of Chemical Physics* **2009**, *131*, 244706.

(33) Hamaker, H. C. The London–van der Waals attraction between spherical particles. *Physica* **1937**, *4*, 1058 – 1072.

(34) Wolff, J.; Komura, S.; Andelman, D. Budding of domains in mixed bilayer domains. *Physical Review E* **2015**, *91*, 012708.

(35) Lipowsky, R. Budding of membranes induced by intramembrane domains. *Journal de Physique II* **1992**, *2*, 1825 – 1840.

(36) Lipowsky, R. Domain-induced budding of fluid membranes. *Biophysical Journal* **1993**, *64*, 1133 – 1138.

(37) Helfrich, W. Elastic Properties of Lipid Bilayers: Theory and Possible Experiments. *Zeitschrift fur Naturforschung C* **1973**, *208*, 214 – 224.

(38) Bahrami, A. H.; Raatz, M.; Agudo-Canalejo, J.; Michel, R.; Curtis, E. M.; Hall, C. K.; Gradielski, M.; Lipowsky, R.; Weikl, T. R. Wrapping of nanoparticles by membranes. *Advances in Colloid and Interface Science* **2014**, *208*, 214 – 224.

(39) Dalke, H. W.; Schulten, K. VMD - Visual Molecular Dynamics. *Journal of Molecular Graphics* **1996**, *14*, 33 – 38.

(40) Tian, A.; Johnson, C.; Wang, W.; Baumgart, T. Line tension at fluid membrane domain boundaries measured by micropipette aspiration. *Physical Review Letters* **2007**, *98*, 208102.

(41) Yeonjeong, H.; Katz, L. E.; Liljestrand, M. Distribution of Fullerene Nanoparticles between Water and Solid Supported Lipid Membranes: Thermodynamics and Effects of Membrane Composition on Distribution. *Environmental Science and Technology* **2015**, *49*, 14546.

(42) Brant, J. A.; Labille, J.; Bottero, J. Y.; Wiesner, M. R. Characterizing the impact of preparation method on fullerene cluster structure and chemistry. *Langmuir* **2006**, *22*, 3878 – 3885.

(43) Palmieri, B.; Grant, M.; Afran, S. A. Prediction of the Dependence of the Line Tension on the Composition of Lineactants and the Temperature in Phase Separated Membranes. *Physical Review Letters* **2014**, *30*, 11734 – 11745.

(44) Schwarzer, R.; Levental, I.; Gramatica, A.; Scolari, S.; Buschmann, V.; Veit, M.; Herrmann, A. The cholestrol-binding motif of the HIV-1 glycoprotein gp41 regulates lateral sorting and oligomerization. *Cellular Microbiology* **2014**, *16*, 1565 – 1581.

(45) Coskun, U.; Gryznek, M.; Dreshsel, D.; Simons, K. Regulation of human EGF receptor by lipids. *Proceedings of the National Academy of Sciences of the United States of America* **2010**, *108*, 9044 – 9048.

(46) Contreras, F. X.; Ernst, A. M.; Haberkant, P.; Bjorkholm, P.; Landahl, E.; Gonen, B.; Tischer, C.; Elofsson, A.; von Heijne, G.; Thiele, C.; Pepperkok, R.; Wieland, F.; Brugger, B. Molecular recognition of a single sphingolipid species by a protein's transmembrane domain. *Nature 481*, 525 – 529.

(47) Ruiz-Herrero, T.; Hagan, M. F. Simulations Show that Virus Assembly and Budding Are Faciliated by Membrane Microdomains. *Biophysical Journal* **2015**, *108*, 585 – 595.

(48) Lazaro, G. L.; Mukhopadhyay, S.; Hagan, M. F. Why Enveloped Viruses Need Cores - The Contribution of a Nucleocapsid Core to a Viral Budding. *Biophysical Journal* **2018**, *114*, 619 – 630.

(49) Yang, S.; Kiessling, V.; Simmons, J. A.; White, J. M.; Tamm, L. K. HIV gp41-mediated membrane fusion occurs at edges of cholesterol-rich lipid domains. *Nature Chemical Biology* **2015**, *11*, 424.

(50) Madsen, J. J.; Grime, J. M. A.; Rossman, J. S.; Voth, G. A. Entropic forces drive clustering and spatial localization of influenza A M2 during viral budding. *Proceedings of the National Academy of Sciences of the United States of America* **2018**, *115*, E8595 – E8603.

(51) G.Khelashvili,; Kollmitzer, B.; Heftberger, P.; Pabst, G.; Harries, D. Calculating the Bending Modulus for Multicomponent Lipid Membranes in Different Thermodynamic Phases. *Journal of Chemical Theory and Computation* **2007**, *91*, 258103.

(52) Li, Z.; Gorfe, A. A. Modulation of a Small Two-Domain Lipid Vesicle by Linactants. *The Journal of Physical Chemistry B* **2014**, *118*, 9208 – 9036.

Graphical TOC Entry

Some journals require a graphical entry for the Table of Contents. This should be laid out "print ready" so that the sizing of the text is correct.

Inside the `tocentry` environment, the font used is Helvetica 8 pt, as required by *Journal of the American Chemical Society*.

The surrounding frame is 9 cm by 3.5 cm, which is the maximum permitted for *Journal of the American Chemical Society* graphical table of content entries. The box will not resize if the content is too big: instead it will overflow the edge of the box.

This box and the associated title will always be printed on a separate page at the end of the document.